



# Selective laser melting (SLM) of AISI 316L—impact of laser power, layer thickness, and hatch spacing on roughness, density, and microhardness at constant input energy density

Sebastian Greco<sup>1</sup> · Kevin Gutzeit<sup>1</sup> · Hendrik Hotz<sup>1</sup> · Benjamin Kirsch<sup>1</sup> · Jan C. Aurich<sup>1</sup>

Received: 6 February 2020 / Accepted: 19 May 2020 / Published online: 28 May 2020  
© The Author(s) 2020

## Abstract

In selective laser melting (SLM) the variation of process parameters significantly impacts the resulting workpiece characteristics. In this study, AISI 316L was manufactured by SLM with varying laser power, layer thickness, and hatch spacing. Contrary to most studies, the input energy density was kept constant for all variations by adjusting the scanning speed. The varied parameters were evaluated at two different input energy densities. The investigations reveal that a constant energy density with varying laser parameters results into considerable differences of the workpieces' roughness, density, and microhardness. The density and the microhardness of the manufactured components can be improved by selecting appropriate parameters of the laser power, the layer thickness, and the hatch spacing. For this reason, the input energy density alone is no indicator for the resulting workpiece characteristics, but rather the ratio of scanning speed, layer thickness, or hatch spacing to laser power. Furthermore, it was found that the microhardness of an additively manufactured material correlates with its relative density. In the parameter study presented in this paper, relative densities of the additively manufactured workpieces of up to 99.9% were achieved.

**Keywords** Additive manufacturing · Selective laser melting · Input energy density · Relative density · Microhardness

## 1 Introduction

Due to the rapid and cost-efficient production of small batches and the freedom of design, additive manufacturing (AM), especially selective laser melting (SLM), is increasingly used in industry [1–4]. In this process, the component is built layer by layer from a metal powder bed [5]. Each layer has a predefined layer thickness, where the powder is melted via a beam, commonly a laser, and subsequently solidifies [6]. The SLM process parameters have a decisive influence on the metallurgical and mechanical properties of the manufactured components [7–9]. Extensive knowledge of the causal relationships between process parameters and component properties is necessary, as these in turn influence the application behavior of the component such as the fatigue strength or wear resistance

[10–14]. For the AM of components from AISI 316L, an austenitic stainless steel which is widely used due to its high corrosion resistance and decent mechanical properties, there is already a broad basis regarding the impact of the SLM process on the component properties, like the roughness [15–18] or the density [19–25]. For example, it was found that an insufficient laser power results in only partial melting of the powder grains. In this case, according to Shen et al. [26] liquid “bridges” are formed between the individual grains and the powder agglomerates. This leads to increased porosity due to the cavities between the powder grains and hence decreased mechanical properties. On the other hand, excessive laser power leads to the evaporation of the material from which keyholes are formed, as investigated by Rai et al. [27]. Hence, if the laser power is too high, the density decreases again. In addition, the dynamics of the melt bath are influenced by the process parameters during SLM and are crucial for the application of new material layers [8]. If the surface tension of the melt bath is high enough, the melt bath may be divided into several small melt beads as a consequence of minimization of its surface energy. This in turn prohibits a uniform application and joining of subsequent material layers on already existing layers [28]. Due to the ball-like shape of the melt beads, this

✉ Sebastian Greco  
sebastian.greco@mv.uni-kl.de

<sup>1</sup> Institute for Manufacturing Technology and Production Systems  
TU Kaiserslautern, Gottlieb-Daimler-Straße,  
67663 Kaiserslautern, Germany

effect of melt bath separation is called balling effect. The balling effect can be reduced by increasing the laser power at simultaneously decreased scanning speed or decreasing the hatch spacing [8, 28].

The correlations of the process parameters used for SLM can ultimately be explained by an input energy density  $E_V$ , linearly correlating with the laser power  $P$ .  $E_V$  can be calculated according to [29] by Eq. (1):

$$E_V = \frac{P}{v_S * S_D * S_A} \quad (1)$$

Thus, increasing the scanning speed  $v_S$ , the layer thickness  $S_D$ , or the hatch spacing  $S_A$  has a reciprocal effect on melting mechanisms such as balling and keyhole phenomena in comparison to the laser power. In order to adapt the workpiece characteristics for instance to the requirements of an intended application, the process parameters need to be adjusted carefully. It is hence of interest how those parameters impact the workpiece. However, a change also results into a change of the input energy density, which overlays the mechanisms of impact. For this reason, the named process parameters are varied in this study, while the input energy density is kept constant by adapting the scanning speed. Contrary to other investigations, the interrelation of these process parameters and the effects on the workpieces' roughness, density, and microhardness can be examined in detail without the overlaying effect of a changing input energy density in this paper. The resulting surface topography, the density, and the microhardness are analyzed.

## 2 Materials and methods

### 2.1 Additive manufacturing

The workpieces were produced using the additive manufacturing machine tool Mlab Cusing by ConceptLaser.<sup>1</sup> Figure 1 shows the interior view of the building volume during SLM as well as the exterior view of the Mlab Cusing. In addition, a list of technical specifications is provided.

The Mlab Cusing is equipped with a Nd:YAG fiber laser ( $\lambda = 1064 \text{ nm}$ ,  $\delta = 50 \text{ }\mu\text{m}$ ) with a maximum power output of 100 W; the building volume is  $90 \times 90 \times 80 \text{ mm}$ . Powdered 316L was used for the SLM process, with a maximum grain size of  $50 \text{ }\mu\text{m}$  (manufacturer's specifications). The produced geometry for all workpieces was a cube with an edge length of 8 mm. The scan paths that form the build-up layers are initially rotated by  $45^\circ$  to avoid running parallel to the build-up layer contour and are then rotated from layer to layer by  $90^\circ$ . Due to

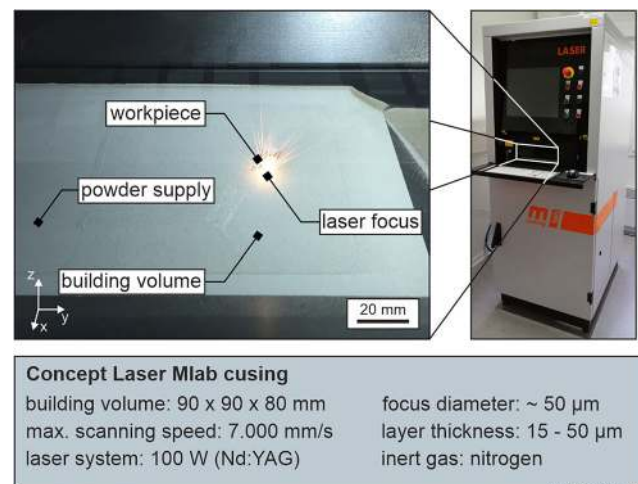


**Fig. 1** Building volume, exterior view, and technical specifications of the SLM machine Mlab Cusing

the scanning strategy (see Tables 1 and 2), the build-up layers are divided into squared exposure fields. Scan vectors of adjacent exposure fields run perpendicular to each other. The workpieces were aligned parallel to the build platform ( $XY$ -plane). During additive manufacturing, the workpieces were fixed to the build platform with 16 cone-shaped supports ( $d = 0.8 \text{ mm}$ ). The supports were arranged at intervals of  $2.4 \text{ mm}$  in  $x$ - and  $y$ -directions ( $\Delta x$  and  $\Delta y$ ) and had a height of  $4 \text{ mm}$  ( $Z$ -direction). The orientation of the workpieces on the building platform, the build-up direction, and the build-up layers are shown in Fig. 2. In order to provide statistical validation, all workpieces were produced three times.

To analyze the influence of the laser power  $P$ , layer thickness  $S_D$ , and hatch spacing  $S_A$  on the workpieces' roughness, density, and microhardness, the process parameters of additive manufacturing were varied. During this variation, a constant input energy density  $E_V$  was achieved by adjusting the scanning speed  $v_S$  of the laser between 100 and 2000 mm/s.

The variation of process parameters during additive manufacturing was subdivided into two parts. First, the influence of layer thickness and laser power on the resulting workpiece characteristics were investigated at a constant hatch spacing of  $S_A = 56 \text{ }\mu\text{m}$  and two levels of input energy density (see Table 1). This variation of process parameters enables a comparison of different layer thicknesses at identical laser power as well as a comparison of different laser powers at identical layer thickness, both for two levels of input energy density.

In a second step, the influence of the hatch spacing was investigated by using two levels of laser power and input energy density (see Table 2). This variation of the laser power  $P$  and input energy density  $E_V$  enables a comparison between different input energy densities at identical laser power as well as a comparison between different laser powers at an identical input energy density. The layer thickness was set to  $S_D = 25 \text{ }\mu\text{m}$  during the variation of the hatch spacing.

<sup>1</sup> Naming of specific manufacturers is done solely for the sake of completeness and does not necessarily imply an endorsement of the named companies nor that the products are necessarily the best for the purpose.

**Table 1** SLM parameters for variation of layer thickness and laser power

Process parameters	Setup 1	Setup 2	Setup 3
Scanning strategy	Successive chessboard	Successive chessboard	Successive chessboard
Hatch spacing $S_A$	56 $\mu\text{m}$	56 $\mu\text{m}$	56 $\mu\text{m}$
Scanning speed $v_S$	Adjusted accordingly	Adjusted accordingly	Adjusted accordingly
Layer thickness $S_D$	25 $\mu\text{m}$	35 $\mu\text{m}$	45 $\mu\text{m}$
Laser power $P$	30, 50, 70, 90 W	30, 50, 70, 80*, 90 W	30, 50, 70, 80*, 90 W
Input energy density $E_V$	33.3 J/mm <sup>3</sup> , 119.0 J/mm <sup>3</sup>	33.3 J/mm <sup>3</sup> , 119.0 J/mm <sup>3</sup>	33.3 J/mm <sup>3</sup> , 119.0 J/mm <sup>3</sup>

\*Laser power  $P = 80$  W was only used for  $E_V = 33.3$  J/mm<sup>3</sup>

The contour and the support structures were exposed with a laser power of  $P = 60$  W and a scanning speed of  $v_S = 600$  mm/s, detached from the layer thickness of the respective process parameter combination.

### 2.2 Workpiece characterization

After SLM, the samples were mechanically removed from the platform. The as-build surface roughness was evaluated over a distance of  $l_n = 4$  mm ( $\lambda_c = 0.8$  mm) using the stylus instrument MarSurf M300 by Mahr GmbH<sup>1</sup>. For statistical verification, three measurements were carried out for each sample, both at the surface perpendicular to the build-up direction ( $XY$ -plane) and at a surface parallel to the build-up direction ( $YZ$ -,  $XZ$ -plane).

The relative density is a comparative value that refers to the ideal material that is free of pores. Therefore, a relative density of 100% describes a completely dense material, which in turn contains a porosity of 0%. The relative density was determined according to Eq. (2), with  $\Delta x$ ,  $\Delta y$ ,  $\Delta z$  describing the workpiece dimensions, the workpiece mass  $m$ , and the density of the material (completely dense)  $\rho_{316L} = 7.99$  g/cm<sup>3</sup> [30]. A cuboid was assumed to calculate the volume. In order to justify this assumption, the samples were milled on each side with an infeed of 0.1 mm so that a defined surface and volume was produced. In addition, the area of the contour scan was also removed by this milling, which led to the fact that only material volumes with varied SLM parameters were considered when determining the relative density. The side lengths of the cuboid were determined via a digital vernier height gauge ( $\pm 0.01$  mm; BZT Maschinenbau GmbH<sup>1</sup>), whereas the mass of the sample was determined by using a

precision balance ( $\pm 0.001$  g; KERN & SOHN GmbH, EMB 200-3<sup>1</sup>).

$$\rho = 100\% \cdot \frac{m}{\Delta x \cdot \Delta y \cdot \Delta z \cdot \rho_{316L}} \tag{2}$$

After the completion of the non-destructive measurements, the samples were prepared for the microhardness measurements. For this purpose, cross sections were prepared at the center of the sample using the Mecatome T210 precision cutting machine<sup>1</sup>. During separation, the thermal–mechanical load was kept low by choosing a low feed rate ( $u_f = 0.03$  mm/min) and assuring constant cooling. Afterwards, the separated samples were embedded. Fine-grained abrasive paper was used in a down grinding processes (P1200, P2500, P4000) with a head rotational speed of  $n_H = 60$  min<sup>-1</sup> and a working rotational speed of  $n = 300$  min<sup>-1</sup>. Subsequently, the samples were polished ( $n = 150$  min<sup>-1</sup>) in a two-stage polishing process by using a 3- $\mu\text{m}$  and a 1- $\mu\text{m}$  diamond suspension. Grinding and polishing were done by using the Mecatech 334 by Presi GmbH<sup>1</sup>.

The microhardness was characterized in two planes, one parallel to the build-up direction ( $YZ$ -plane) and the other one perpendicular to the build-up direction ( $XY$ -plane) (Fig. 3a). The Vickers microhardness was determined according to DIN EN ISO 6507-1 [31] with the microhardness tester MicroMet 5100 by Bühler AG<sup>1</sup> at a test load of  $F = 0.098$  N (HV0.01). In order to achieve local hardness values, the microhardness was determined over a total of five measuring areas, according to Fig. 3b. For statistical purposes, a total of four measurements were carried out in each measuring area, summing up to a total of 40 measurements per workpiece.

**Table 2** SLM parameters for variation of hatch spacing

Process parameters	Setup 4	Setup 5	Setup 6
Scanning strategy	Successive chessboard	Successive chessboard	Successive chessboard
Layer thickness $S_D$	25 $\mu\text{m}$	25 $\mu\text{m}$	25 $\mu\text{m}$
Hatch spacing $S_A$	42, 56, 70, 84 $\mu\text{m}$	42, 56, 70, 84 $\mu\text{m}$	42, 56, 70, 84 $\mu\text{m}$
Laser power $P$	50 W	50 W	70 W
Input energy density $E_V$	33.3 J/mm <sup>3</sup>	119.0 J/mm <sup>3</sup>	33.3 J/mm <sup>3</sup>
Scanning speed $v_S$	Adjusted accordingly	Adjusted accordingly	Adjusted accordingly

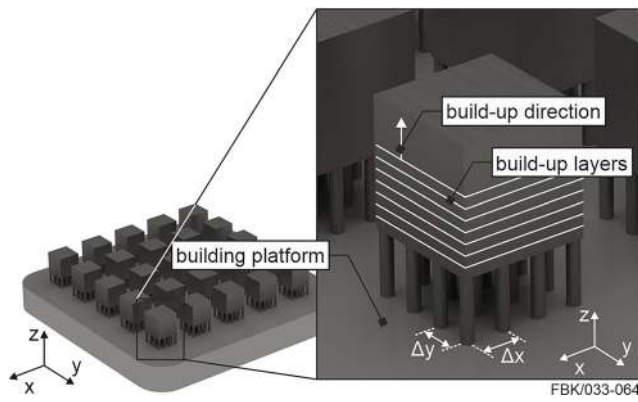


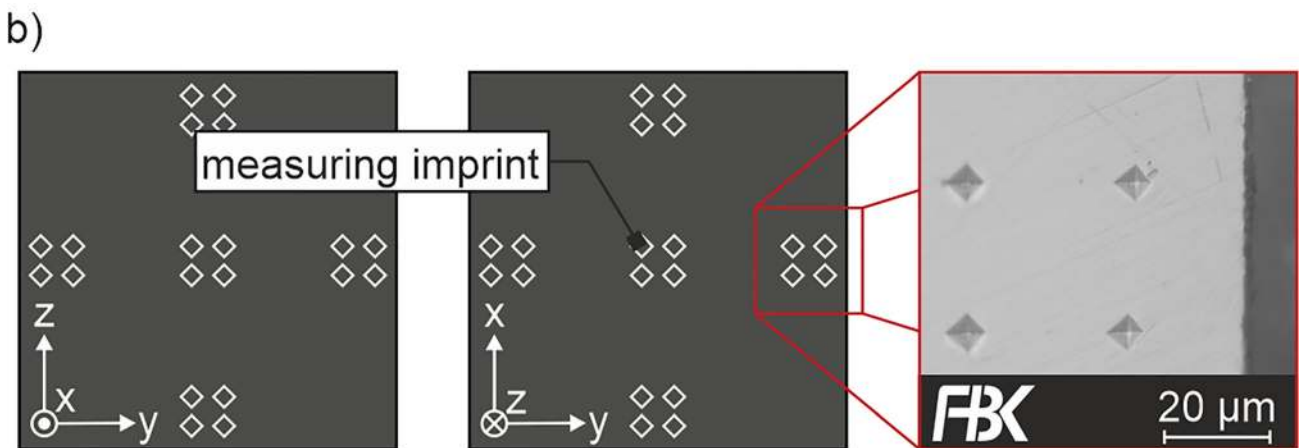
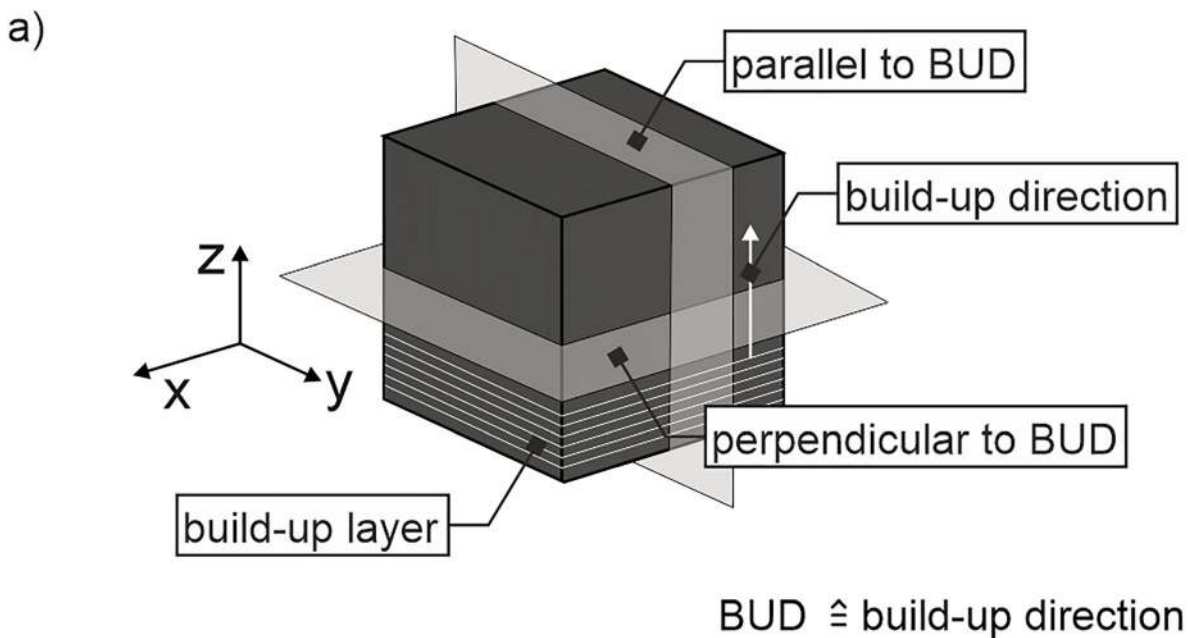
Fig. 2 Building platform, workpiece orientation, and support structures

The given standard deviations are the mean value of the standard deviations of all measuring points belonging to one process parameter combination. The number of repetitions of each measuring point is three with respect to the relative density, nine with respect to the roughness, and 40 with respect to the microhardness.

### 3 Results and discussion

#### 3.1 Variation of layer thickness and laser power

In the following, the influence of layer thickness and laser power on the as-build surface roughness, relative density, and microhardness is shown at a constant hatch spacing of  $S_A = 56 \mu\text{m}$ .



FBK/033-041

Fig. 3 a Workpiece separation in planes parallel and perpendicular to the build-up direction. b Measurement pattern for microhardness



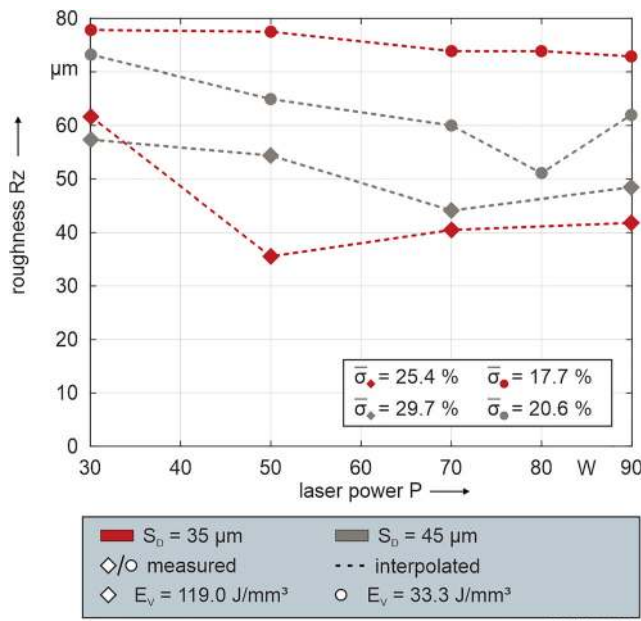


Fig. 4 Average roughness Rz for different laser power P, layer thickness  $S_D$ , and input energy density  $E_V$  at surface perpendicular to the build-up direction (XY-plane)

### 3.1.1 Roughness

The average roughness at the surface perpendicular to the build-up direction of the workpieces (XY-plane) is shown in Fig. 4 as a function of laser power P, layer thickness  $S_D$ , and input energy density  $E_V$ .

When comparing the values shown in Fig. 4, a significant decrease in surface roughness can be observed with increasing input energy density, especially for  $S_D = 35 \mu\text{m}$ . Taking the values of the standard deviation into account, at constant input energy density, the influence of the layer thickness and the laser power on the surface roughness can be considered as comparably small. However, there is a tendency that the average roughness slightly decreases with increasing laser power. Figure 5 exemplarily shows the as-build surface perpendicular to the build-up direction (XY-plane) for high and low input energy density. In case of a low input energy density, it can be seen that spherical structures are formed on the workpiece’s surface. Due to the comparatively low input energy density, these structures can be interpreted as unmelted or only partially melted powder grains and thus as a consequence of poor dynamics of the melt path and the occurrence of the balling effect. This assumption is confirmed by the values shown in Fig. 4, in which all values regarding Rz are above the specified maximum grain size of  $50 \mu\text{m}$ .

On the other hand, it can be seen that by increasing the input energy density, independent of the variations of layer thickness and laser power, the roughness within the surface perpendicular to the build-up direction can be reduced. Due to the higher input of thermal energy per volume, more powder material is melted, which also prevents the balling effect. In this case, the dynamics of the melt path and the flow of melt can be assumed to be more suitable for the generation of less rough surfaces, which is confirmed by the measured values of Rz for  $E_V = 119.0 \text{ J/mm}^3$  (see Fig. 4).

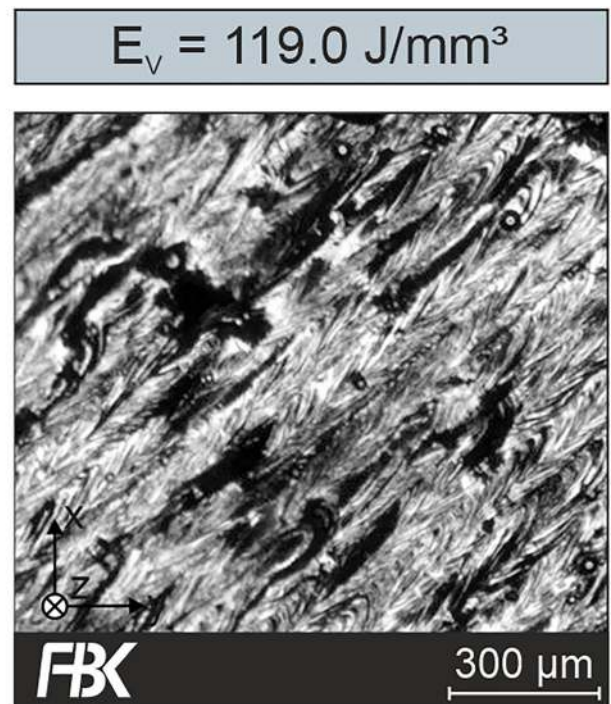
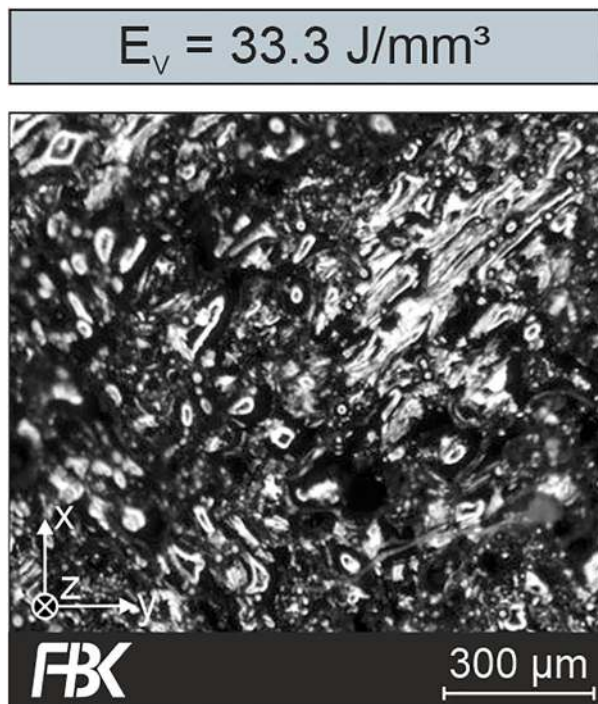


Fig. 5 As-build surfaces perpendicular to the build-up direction (XY-plane) for  $E_V = 33.3 \text{ J/mm}^3$  and  $E_V = 119.0 \text{ J/mm}^3$

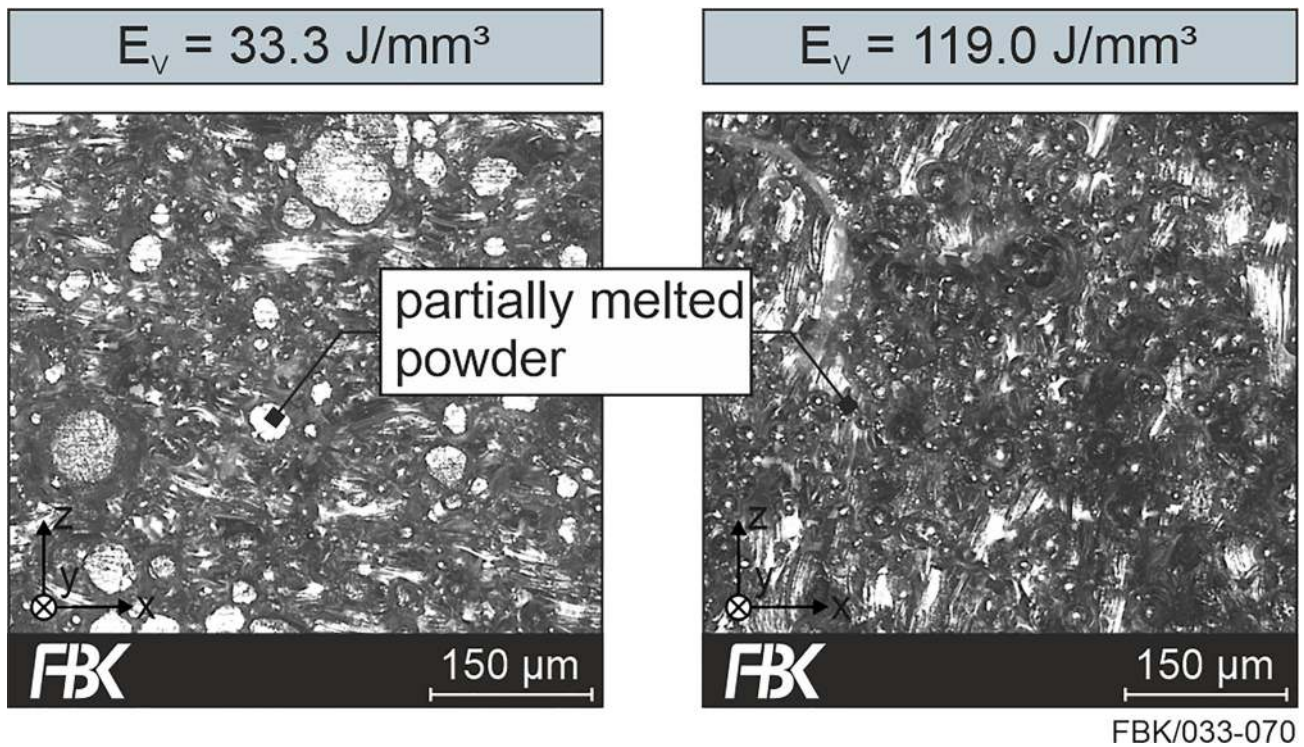


Fig. 6 As-build surfaces parallel to the build-up direction ( $XZ$ -plane) for  $E_V = 33.3 \text{ J/mm}^3$  and  $E_V = 119.0 \text{ J/mm}^3$

In contrast to the shown differences in roughness, no significant influence of the examined process parameters can be observed when regarding the surfaces parallel to the build-up direction ( $XZ$ - and  $YZ$ -plane). This is due to the temperature gradient along the  $XY$ -plane. During SLM, the workpiece is divided into several build-up layers ( $XY$ -plane), which are heated by the laser. The heat of the melted powder is dissipated into the powder bed, causing the prevailing temperature in the powder bed to decrease in  $X$ ,  $Y$ , and  $Z$  direction with increasing distance to the laser-exposed powder. Consequently, regardless of the melting bath temperature, there is always a certain distance  $\Delta x$  and  $\Delta y$  from the boundary of the build-up layer beyond which the temperature is no longer sufficient during laser exposure of the boundary to completely melt the powder. At this point, powder grains are only partially molten and are thus welded to the build-up layer contour, forming the workpiece surfaces parallel to the build-up direction. The partially melting of powder on a surface parallel to the build-up direction ( $XZ$ -plane) is shown in Fig. 6 for both input energy densities used. The roughness of the surfaces parallel to the build-up direction ( $R_z = 57.9 \pm 7.4 \mu\text{m}$ ) is therefore defined by the powder grain size of the powder used during SLM.

### 3.1.2 Relative density

In Fig. 7 the relative density in dependence of the examined parameters is depicted. It can be seen that denser samples are produced at a higher input energy density. Due to the higher

amount of thermal energy, a larger percentage of material within the volume can be heated above its melting point, thus less material remains unmelted or only partially melted, which increases the relative density.

Furthermore, the relative density increases when a higher laser power is used. This behavior can be observed

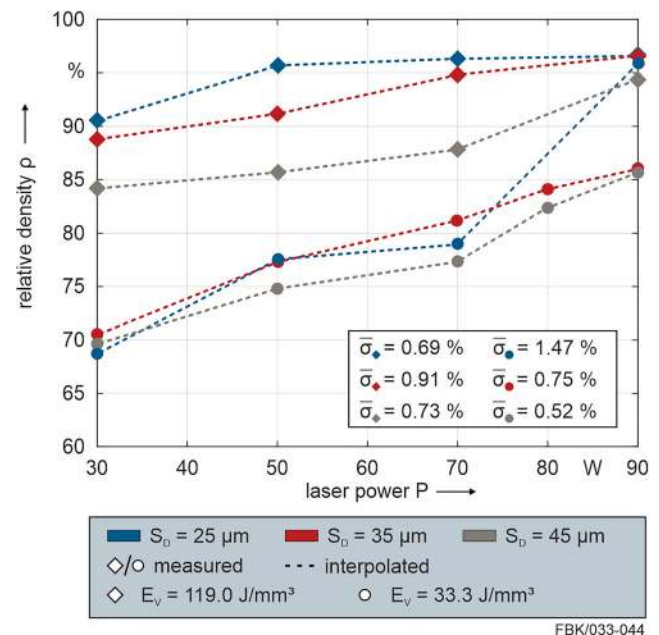


Fig. 7 Relative density  $\rho$  for different laser power  $P$ , layer thickness  $S_D$ , and input energy density  $E_V$



independently of the other varied parameters. Note that, in this paper, two levels of input energy densities were compared, while a constant input energy density was assured; hence, a higher laser power must be compensated by a faster scanning speed. Due to this, when increasing the laser power, the same volume of powder has to absorb the same amount of thermal energy in a shorter time interval in order to be melted. As the effect of a higher laser power is leading to a higher relative density, which is shown for both input energy densities, the increase of relative density may be attributed to a better ratio between supplied laser power and heat conduction. However, as the relative density of all measurements is increasing with increasing laser power, the available time is still sufficient to distribute the energy in such a way that more powder material can be heated above its melting point. It can be assumed that the increase of relative density due to increased laser power has a boundary that depends on material properties such as the thermal conductivity.

In addition, the values shown in Fig. 6 indicate a decrease in relative density with increasing layer thickness at  $E_V = 119.0 \text{ J/mm}^3$ . Considering a constant input energy density, the decrease of the relative density at higher layer thicknesses may be explained by a limited depth of penetration of the laser's energy into the powder bed. Although the scanning speed compensates the increased layer thickness and the same amount of energy per volume is absorbed, the energy, which is mainly absorbed by the top powder layer, has to be transferred directly to the layer below. Within a certain limit, this is intended to partially melt the lower layer in order to create layer adhesion. With increasing layer thickness and thus a larger powder volume (in negative Z-axis) to be melted, the boundary of the molten powder volume increases. This may lead to an insufficient amount of energy or temperature with increasing distance to the powder surface in negative Z-direction, resulting in insufficient melting of not yet melted powder or already melted layers. Since both melting processes are required to create a new

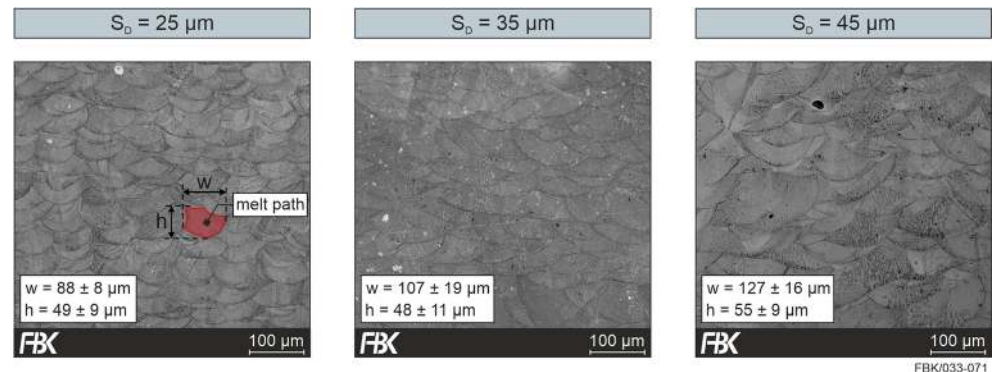
build-up layer and to join the just melted layer with already existing build-up layers, an increased layer thickness results in a lower relative density. To illustrate the laser's limited depth of penetration, etched micrographs of the cross-sections parallel to the build-up direction ( $XZ$ -plane) are shown in Fig. 8 for different layer thicknesses. In addition, the determination of the melt path width  $w$  and height  $h$  is shown exemplarily on one melt path; the measurements to determine the absolute values of  $w$  and  $h$  were carried out on 20 melt paths. Regarding the melt path width and height it can be seen that with increasing layer thickness only the melt path width increases. The melt path height changes only slightly with varying layer thickness, which demonstrates the laser's limited depth of penetration even though using process parameters that consider an increased layer thickness.

Due to the generally lower amount of absorbed energy and thus generally poor joining of just melted and already existing build-up layers when applying an input energy density of  $E_V = 33.3 \text{ J/mm}^3$ , the effect of the layer thickness on the relative density is reduced compared to  $E_V = 119.0 \text{ J/mm}^3$ . Applying the low input energy density  $E_V = 33.3 \text{ J/mm}^3$ , the impact of laser power on the relative density of the workpieces appears more significant.

Further, the gradients of the interpolated curves showing the relative density of  $E_V = 119.0 \text{ J/mm}^3$  seem to indicate an improvement towards a particularly favorable ratio of laser power, scanning speed, and layer thickness for  $S_D = 25 \text{ }\mu\text{m}$  between 30 and 50 W,  $S_D = 35 \text{ }\mu\text{m}$  between 50 and 70 W, and for  $S_D = 45 \text{ }\mu\text{m}$  between 70 and 90 W.

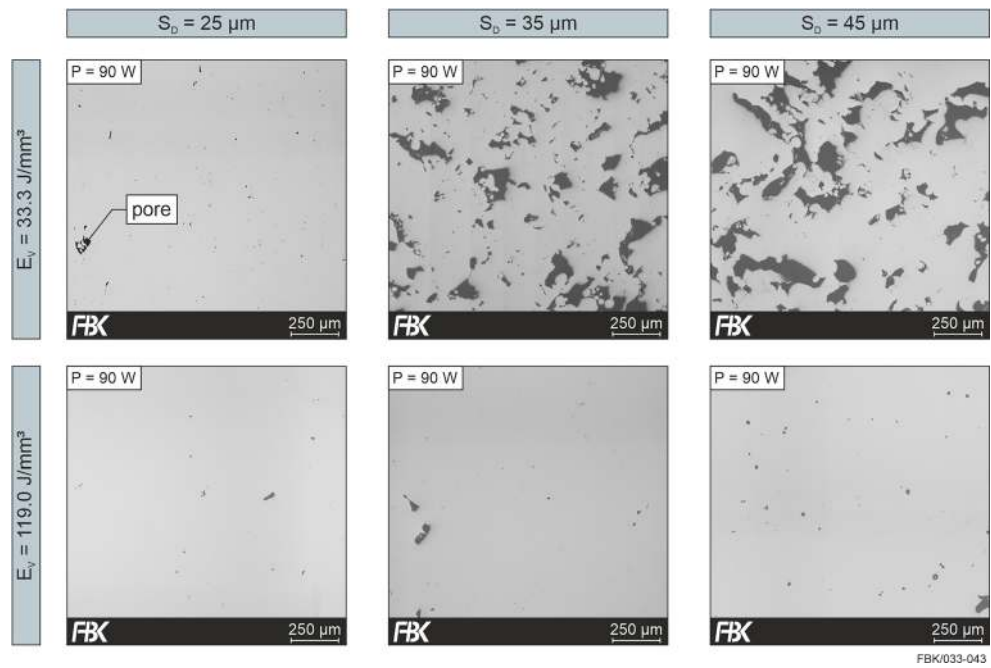
The described influence of input energy density on the relative density of workpieces produced by SLM can be seen on the micrographs of the workpiece's cross sections ( $XY$ -plane) in Fig. 9. It can be clearly seen that the relative density increases with higher input energy density and decreases with increasing layer thickness, which confirms the assumptions above.

**Fig. 8** Etched micrographs of the cross-sections ( $XZ$ -plane) for different layer thickness  $S_D$ ,  $E_V = 119.0 \text{ J/mm}^3$ ,  $S_A = 56 \text{ }\mu\text{m}$



FBK/033-071

**Fig. 9** Micrographs of the cross-sections (*XY*-plane) for different layer thickness  $S_D$  and input energy density  $E_V$ ,  $S_A = 56 \mu\text{m}$



**3.1.3 Microhardness**

In Fig. 10 the microhardness of the additively manufactured workpieces at different layer thicknesses and input energy densities is shown.

The microhardness of all additively manufactured workpieces varies between 232 and 275 HV 0.01, which is similar to the results of additively manufactured workpieces by Cherry et al. [32] and Tolosa et al. [33] but is

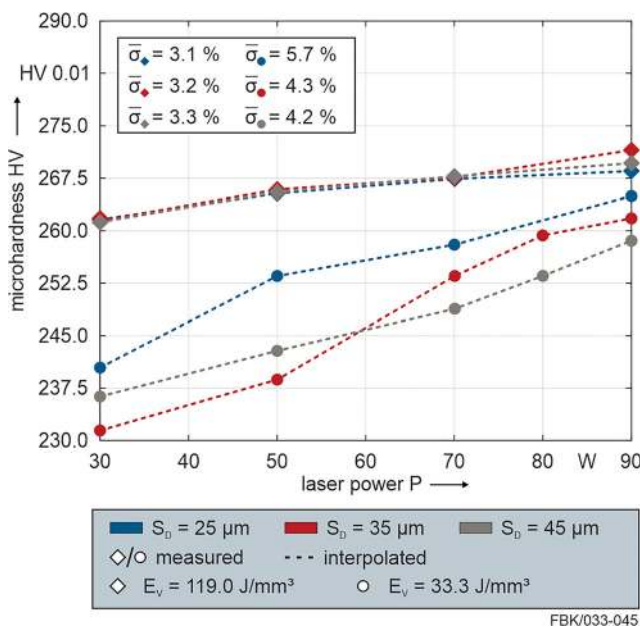


**Fig. 10** Hardness for different laser power  $P$ , layer thickness  $S_D$ , and input energy density  $E_V$

significantly higher than the microhardness of casted, rolled, solution-annealed, and water quenched reference material (218 HV 0.01 [34]). This increased hardness compared to reference material is due to the already known, directed microstructure of additively manufactured workpieces [35].

An increase in microhardness with increasing laser power can be observed for all layer thicknesses  $S_D$  and input energy densities  $E_V$ . The workpieces manufactured at the higher input energy density  $E_V = 119.0 \text{ J/mm}^3$  generally show higher values of microhardness compared to the workpieces produced at  $E_V = 33.3 \text{ J/mm}^3$  with identical laser power and layer thickness. No influence of the layer thickness on the microhardness can be determined for workpieces produced at  $E_V = 119.0 \text{ J/mm}^3$ , while workpieces produced with lower input energy density show a trend towards decreasing microhardness with increasing layer thickness.

In Fig. 11 the microhardness for all analyzed process parameter combinations (setups 1-3) in relation to their corresponding relative density is shown. Applying the same input energy density results in similar relative densities independent of the respective other AM parameters. In addition, the representation given in Fig. 11 reveals a second-order correlation between microhardness and relative density, indicating an increase in microhardness with increasing relative density. The approximated equation indicates a theoretical maximum microhardness of 270 HV 0.01 at a relative density of 102.8%. The determined regression is only valid within the investigated test frame.



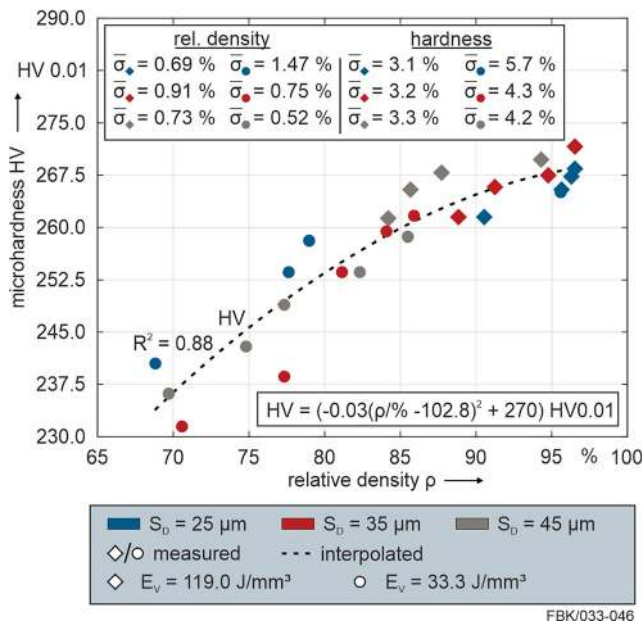


Fig. 11 Correlation between hardness and relative density for different laser power  $P$ , layer thickness  $S_D$ , and input energy density  $E_V$

The increased microhardness of workpieces with a higher density is due to their associated lower porosity. A higher relative density, respectively a lower porosity, results in a higher percentage of material being available to counteract the indentation of the test specimen during hardness measurements. On the other hand, pores located below the surface reduce the stiffness of the workpiece locally as the test specimen can penetrate deeper into the material. Therefore, increased relative density leads to increased resistance of the material against deformation and thus results in increased microhardness.

### 3.2 Variation of hatch spacing

In the following, the influence of the hatch spacing  $S_A$  on the relative density and microhardness is described. For this purpose, workpieces produced using process parameter combination setups 4–6 (see Table 2) are analyzed.

In Fig. 12 etched micrographs of the cross-sections perpendicular to the build-up direction of the additively manufactured workpieces ( $XY$ -plane) at high input energy density

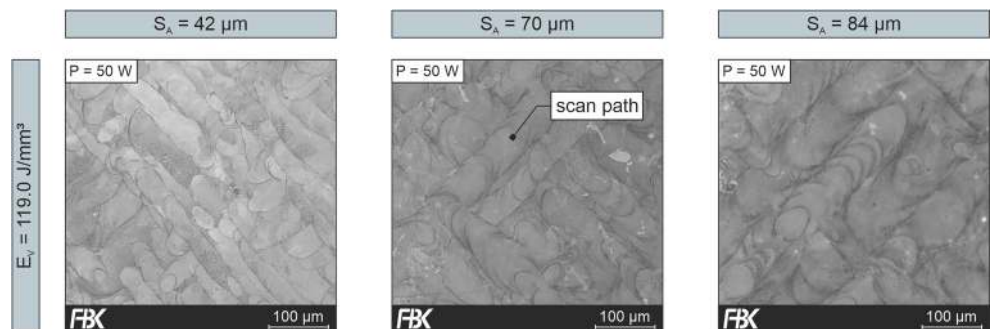
$E_V = 119.0 \text{ J/mm}^3$  and constant laser power  $P = 50 \text{ W}$  are shown. The differently oriented scan paths seen within one cross-section are due to the perpendicular orientation of scan paths of adjacent exposure fields defined by the scanning strategy. The comparison of the etched micrographs (left to right) shows the increase of hatch spacing defined during SLM.

The influence of the hatch spacing on the relative density and the microhardness is shown in Fig. 13 at different laser powers and input energy densities. At a laser power of  $P = 50 \text{ W}$ , the relative density increases for both levels of input energy density with increasing hatch spacing. In contrast, the relative density of workpieces produced at  $P = 70 \text{ W}$  and  $E_V = 33.3 \text{ J/mm}^3$  initially decreases when the hatch spacing increases, but then increases after a hatch spacing of  $S_A = 70 \mu\text{m}$ .

The increase of relative density with increasing hatch spacing may be attributed to the ratio of laser power  $P$  and scanning speed  $v_s$ . Due to the compensation of the input energy density by adjusting the scanning speed, larger hatch spacing (increased from 42 to 84  $\mu\text{m}$ ) results in a lower scanning speed (reduced by factor 2, see Eq. (1)). Therefore, despite constant input energy density, more time is available to absorb the same amount of energy. The hatch spacing only defines the distance of two adjacent scan paths of the laser and thus the width of the volume that has to be melted. But as the surface that is exposed to the laser is constant, determined by the diameter of the laser focus ( $\delta = 50 \mu\text{m}$ ), a decreased scanning speed results into a longer heat impact. This longer time interval leads to more heat being distributed into the surrounding powder. This improved heat distribution in turn results in the melting of a larger amount of powder and thus to an increase in relative density. In conclusion, the high relative density of the workpieces produced with  $P = 70 \text{ W}$ ,  $E_V = 33.3 \text{ J/mm}^3$ , and  $S_A = 42 \mu\text{m}$  compared to  $S_A = 70 \mu\text{m}$  and  $S_A = 84 \mu\text{m}$  (red line) may be attributed to a more appropriate ratio of process parameters.

The microhardness of the additively manufactured materials shown in Fig. 13 again reproduces the profile of the relative density, which is due to the already shown correlation between relative density and microhardness (see Fig. 11).

Fig. 12 Etched micrographs of the cross-sections ( $XY$ -plane) for different hatch spacing  $S_A$ ,  $E_V = 119.0 \text{ J/mm}^3$ ,  $S_D = 25 \mu\text{m}$



FBK/033-049

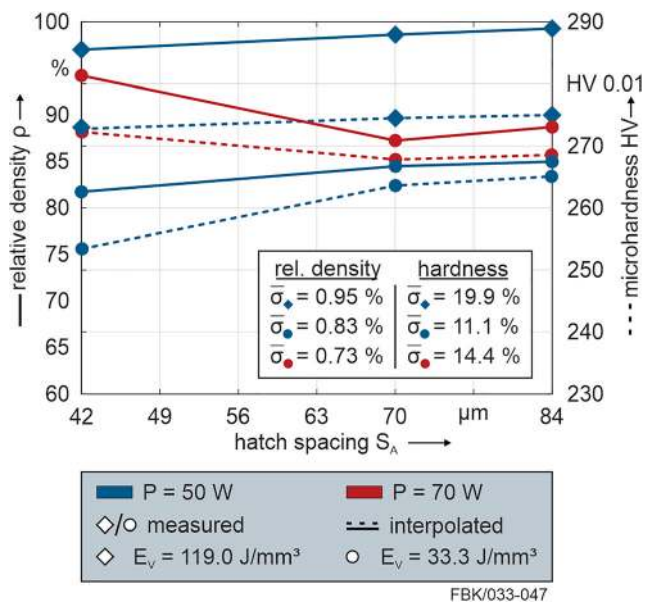


**Fig. 13** relative density  $\rho$  and hardness for different laser power  $P$ , hatch spacing  $S_A$ , and input energy density  $E_v$

## 4 Conclusion and outlook

The research presented in this paper focuses on the effects of process parameter combinations used during SLM of AISI 316L. The process parameters laser power, layer thickness, and hatch spacing were varied in two studies using process parameter combination setups 1–3 for the variation of laser power and layer thickness and setups 4–6 for the variation of hatch spacing. In order to ensure similar process conditions, the input energy density was kept constant by compensating the variation of the three named process parameters via the adjustment of the scanning speed. Two levels of input energy density were examined. The additively manufactured workpieces were characterized on the basis of their relative density, microhardness, and surface roughness.

Based on the experimental results, the following general conclusions can be drawn:

- Input energy density alone is no indicator for the resulting workpiece characteristics, but rather the ratio of scanning speed, layer thickness, or hatch spacing to laser power.
- The heat dissipation and distribution as well as the time available for heat dissipation and distribution is crucial.
- The microhardness of AISI 316L manufactured by SLM increases with increasing relative density.
- The roughness of the surface perpendicular to the build-up direction can be influenced by a variation of the process parameters.
- The roughness of the surfaces parallel to the build-up direction is independent of the process parameters and thus, due to partially melted powder grains, is defined by the grain diameter of the used powder.

Furthermore, at a constant input energy density, the following process parameter correlations can be found for the parameter range investigated in this study:

- An increasing laser power leads to a decreased roughness at the surface perpendicular to the build-up direction, increased relative density, and therefore increased microhardness.
- Due to the limited depth of penetration of the laser's energy into the powder bed, a higher layer thickness leads to a decreased relative density and decreased microhardness.
- Increasing the hatch spacing leads to increasing relative density and microhardness.

In further investigations, more data regarding relative density as a function of process parameters will be generated in order to determine the correlations between the process parameters during SLM and the workpiece characteristics of the manufactured AISI 316L in further detail by means of machine learning. Furthermore, suitable finishing methods and their impact on the surface integrity and the fatigue behavior will also be investigated.

**Funding information** This research was funded by the State Research focus “Advanced Materials Engineering (AME)” at the Technische Universität Kaiserslautern. The authors also received support from the KSB Stiftung for the research project 1.1352.2019.1 “OptiAM—Gestaltung additiv-subtraktiver Prozessketten der Fertigung.” Open Access funding provided by Projekt DEAL.

**Open Access** This article is licensed under a Creative Commons Attribution 4.0 International License, which permits use, sharing, adaptation, distribution and reproduction in any medium or format, as long as you give appropriate credit to the original author(s) and the source, provide a link to the Creative Commons licence, and indicate if changes were made. The images or other third party material in this article are included in the article's Creative Commons licence, unless indicated otherwise in a credit line to the material. If material is not included in the article's Creative Commons licence and your intended use is not permitted by statutory regulation or exceeds the permitted use, you will need to obtain permission directly from the copyright holder. To view a copy of this licence, visit <http://creativecommons.org/licenses/by/4.0/>.

## References

1. Riveiro A, del Val J, Comesaña R, Lusquiños F, Quintero F, Boutinguiza M, Pou J (2019) Laser additive manufacturing processes for near net shape components, in: Dr. G. Kapil (Eds.), Near net shape manufacturing processes, Springer, Cham, pp. 105–141. [https://doi.org/10.1007/978-3-030-10579-2\\_5](https://doi.org/10.1007/978-3-030-10579-2_5)
2. Klier R, Piller FT (2019) Local manufacturing and structural shifts in competition: market dynamics of additive manufacturing. *Int J Prod Econ* 216:23–34. <https://doi.org/10.1016/j.ijpe.2019.04.019>
3. Ngo TD, Kashani A, Imbalzano G, Nguyen KTQ, Hui D (2018) Additive manufacturing (3D printing): a review of materials, methods, applications and challenges. *Composites Part B: Engineerin* 143:172–196. <https://doi.org/10.1016/j.compositesb.2018.02.012>

4. Li N, Huang S, Zhang G, Qin R, Liu W, Xiong H, Shi G, Blackburn J (2019) Progress in additive manufacturing on new materials: a review. *J Mater Sci Technol* 35:242–269. <https://doi.org/10.1016/j.jmst.2018.09.002>
5. Islam M, Purtonen T, PiiliH H, Salminen A, Nyrhilä O (2013) Temperature profile and imaging analysis of laser additive manufacturing of stainless steel. *Phys Procedia* 41:835–842. <https://doi.org/10.1016/j.phpro.2013.03.156>
6. Nagarajan B, Hu Z, Song X, Zhai W, Wei J (2019) Development of micro selective laser melt-ing: the state of the art and future perspectives. *Engineering* 5:702–720. <https://doi.org/10.1016/j.eng.2019.07.002>
7. Peng T, Chen C (2018) Influence of energy density on energy demand and porosity of 316L stainless steel fabricated by selective laser melting. *Int J Precis Eng Manuf Technol* 5(1):55–62. <https://doi.org/10.1007/s40684-018-0006-9>
8. Li R, Liu J, Shi Y, Wang L, Jiang W (2012) Balling behavior of stainless steel and nickel powder during selective laser melting process. *Int J Adv Manuf Technol* 59(9–12):1025–1035. <https://doi.org/10.1007/s00170-011-3566-1>
9. Kamath C, El-dasher B, Gallegos GG, King WE, Sisto A (2014) Density of additively-manufactured, 316L SS parts using laser powder-bed fusion at powers up to 400W. *Int J Adv Manuf Technol* 74(1–4):65–78. <https://doi.org/10.1007/s00170-014-5954-9>
10. Nadot Y, Nadot-Martin C, Kan WH, Boufadene S, Foley M, Cairney J, Proust G, Ridosz L (2019) Predicting the fatigue life of an AISi10Mg alloy manufactured via selective laser melting by using data from computed tomography. *Addit Manuf*, 100899. <https://doi.org/10.1016/j.addma.2019.100899>
11. Afkhami S, Dabiri M, Alavi SH, Björk T, Salminen A (2019) Fatigue characteristics of steels manufactured by selective laser melting. *Int J Fatigue* 122:72–83. <https://doi.org/10.1016/j.ijfatigue.2018.12.029>
12. Bartolomeu F, Buciumeanu M, Pinto E, Alves N, Carvalho O, Silva FS, Miranda G (2017) 316L stainless steel mechanical and tribological behavior—acomparison between selective laser melting, hot pressing and conventional casting. *Addit Manuf* 16:81–89. <https://doi.org/10.1016/j.addma.2017.05.007>
13. Lopez-Galilea I, Rutttert B, He J, Hammerschmidt T, Drautz R, Gault B, Theisen W (2019) Additive manufacturing of CMSX-4 Ni-base superalloy by selective laser melting: influence of processing parameters and heat treatment. *Addit Manuf* 100874:100874. <https://doi.org/10.1016/j.addma.2019.100874>
14. Li H, Ramezani M, Li M, Ma C, Wang J (2018) Tribological performance of selective laser melted 316L stainless steel. *Tribol Int* 128:121–129. <https://doi.org/10.1016/j.triboint.2018.07.021>
15. Kruth JP, Yasa E, Deckers J, Roughness improvement in selective laser melting, Proceedings of the 3rd international conference on polymers and moulds innovations (2008) 170–183. <https://lirias.kuleuven.be/retrieve/117846>
16. Shrestha R, Simsiriwong J, Sharmsaei N (2019) Fatigue behavior of additive manufactured 316L stainless steel parts: effects of layer orientation and surface roughness. *Addit Manuf* 28:23–28. <https://doi.org/10.1016/j.addma.2019.04.011>
17. Simson T, Emmel A, Dwars A, Böhm J (2017) Residual stress measurements on AISI 316L samples manufactured by selective laser melting. *Addit Manuf* 17:183–189. <https://doi.org/10.1016/j.addma.2017.07.007>
18. Stasic J, Bozic D (2016) The effect of NiB additive on surface morphology and microstructure of 316L stainless steel single tracks and layers obtained by SLM. *Surf Coat Technol* 307A:407–417. <https://doi.org/10.1016/j.surfcoat.2016.09.019>
19. Dadbakhsh S, Hao L, Sewell N (2012) Effect of selective laser melting layout on the quality of stainless steel parts. *Rapid Prototyp J* 18(3):241–249. <https://doi.org/10.1108/13552541211218216>
20. J.P. Kruth, M. Badrossamay, E. Yasa, J. Deckers, L. Thijs, J. Van Humbeeck, Part and material properties in selective laser melting of metals, in: Z. Wansheng, Y. Jun, Z. Di, Proceedings of the 16th international symposium on electromachining, Shanghai Jiao Tong University Press, Shanghai, 2010, pp. 3–14. <https://lirias.kuleuven.be/handle/123456789/265815>
21. Laohaprapanon A, Jeamwattthanachai P, Wongcumchang W, Chantawanich N, Chantaweroad S, Sitthiseripratip K, Wisutmethangoon S (2012) Optimal scanning condition of selective laser melting processing with stainless steel 316L powder. *Adv Mater Res* 341-342:816–820. <https://doi.org/10.4028/www.scientific.net/AMR.341-342.816>
22. Liu B, Wildman R, Tuck C, Ashcroft I, Hague R (2011) Investigation the effect of particle size distribution on processing parameters optimisation in selective laser melting process, in: D.L. Bourell (Ed.), International solid freeform fabrication symposium: an additive manufacturing conference. University of Texas at Austin, Austin, pp. 227–238. [https://www.researchgate.net/publication/268365007\\_Investigation\\_the\\_effect\\_of\\_particle\\_size\\_distribution\\_on\\_processing\\_parameters\\_optimisation\\_in\\_selective\\_laser\\_melting\\_process](https://www.researchgate.net/publication/268365007_Investigation_the_effect_of_particle_size_distribution_on_processing_parameters_optimisation_in_selective_laser_melting_process)
23. Yadroitsev I, Smurov I (2010) Selective laser melting technology: from the single laser melted track stability to 3d parts of complex shape. *Phys Procedia* 5(B):551–560. <https://doi.org/10.1016/j.phpro.2010.08.083>
24. Yasa E, Deckers J, Kruth J (2011) The investigation of the influence of laser re-melting on density, surface quality and microstructure of selective laser melting parts. *Rapid Prototyp J* 17(5):312–327. <https://doi.org/10.1108/13552541111156450>
25. Yakout M, Elbestawi MA, Veldhuis SC (2019) Density and mechanical properties in selective laser melting of Invar 36 and stainless steel 316L. *J Mater Process Technol* 266:397–420. <https://doi.org/10.1016/j.jmatprotec.2018.11.006>
26. Shen YF, Gu DD, Pan YF (2006) Balling process in selective laser sintering 316 stainless steel powder. *Key Eng Mater* 315:357–360. <https://doi.org/10.4028/www.scientific.net/KEM.315-316.357>
27. Rai R, Elmer JT, Palmer T, Roy D (2007) Heat transfer and fluid flow during keyhole mode laser welding of tantalum Ti-6Al-4V, 304L stainless steel and vanadium. *J Phys D Appl Phys* 40(18):5753–5766. <https://doi.org/10.1088/0022-3727/40/18/037>
28. Li R, Shi Y, Wang Z, Wang L, Liu J, Jiang W (2010) Densification behavior of gas and water atomized 316L stainless steel powder during selective laser melting. *Appl Surf Sci* 256(13):4350–4356. <https://www.sciencedirect.com/science/article/pii/S0169433210001947>
29. Sinicio M, Witvrouw A, Dewulf W (2019) Influence of the particle size distribution on surface quality of Maraging 300 parts produced by laser powder bed fusion. Proceedings of the Special Interest Group meeting on Advanced Precision in Additive Manufacturing:31–34. [https://www.researchgate.net/publication/335843076\\_Influence\\_of\\_the\\_particle\\_size\\_distribution\\_on\\_surface\\_quality\\_of\\_Maraging\\_300\\_parts\\_produced\\_by\\_Laser\\_Powder\\_Bed\\_Fusion](https://www.researchgate.net/publication/335843076_Influence_of_the_particle_size_distribution_on_surface_quality_of_Maraging_300_parts_produced_by_Laser_Powder_Bed_Fusion)
30. Capek J, Machova M, Fousova M, Kubasek J, Vojtech D, Fojt J, Jablonska E, Lipov J, Rumi T (2016) Highly porous, low elastic modulus 316L stainless steel scaffold prepared by selective laser melting. *Mater Sci Eng C* 69:631–639. <https://doi.org/10.1016/j.msec.2016.07.027>
31. DIN EN ISO 6507-1. Metallische Werkstoffe: Härteprüfung nach Vickers – Teil 1: Prüfverfahren, Beuth, Berlin, 2018. <https://doi.org/10.31030/2778746>
32. Cherry JA, Davies HM, Mehmood S, Lavery NP, Brown SG, Sienz J (2015) Investigation into the effect of process parameters on microstructural and physical properties of 316L stainless steel parts by



- selective laser melting. *Int J Adv Manuf Technol* 76(5–8):869–879. <https://doi.org/10.1007/s00170-014-6297-2>
33. Tolosa I, Garcíandia F, Zubiri F, Zapirain F, Esnaola A (2010) Study of mechanical properties of AISI 316 stainless steel processed by “selective laser melting,” following different manufacturing strategies. *Int J Adv Manuf Technol* 51(5–8):639–647. <https://doi.org/10.1007/s00170-010-2631-5>
34. Aurich JC, Greco S, Hotz H, Zimmermann M, Hartig J, Kirsch B (2017) Schleifende Nachbearbeitung additiv gefertigter austenitischer Edelmstähle. *ZWF - Zeitschrift für wirtschaftlichen Fabrikbetrieb* 112(7–8):473–476. <https://doi.org/10.3139/104.111748>
35. Yusuf SM, Chen Y, Boardman R, Yang S, Gao N (2017) Investigation on porosity and microhardness of 316L stainless steel fabricated by selective laser melting. *Metals* 7(2):1–12. <https://doi.org/10.3390/met7020064>

**Publisher's note** Springer Nature remains neutral with regard to jurisdictional claims in published maps and institutional affiliations.